ADVANCED SENSOR RESEARCH Open Access
www.advsensorres.com

Highly Sensitive Detection of Human Serum Albumin Biomarker Using a Molecularly Imprinted Polymer-Based Electrochemical Capacitance Sensor

*Heitor F. Trevizan, Pedro C. M. Pizzol, André Olean-Oliveira, Patrícia Monteiro Seraphim, and Marcos F. S. Teixeira**

This work presents a highly sensitive, label-free, and redox probe-free electrochemical sensor for human serum albumin (SA) based on a molecularly imprinted polymer (MIP) of electropolymerized poly(azo-Bismarck Brown Y) on FTO electrodes. Successful imprinting creating specific recognition sites is confirmed spectroscopically and electrochemically. Comparative Electrochemical Impedance/Capacitance Spectroscopy (EIS/ECS) studies between the MIP and a non-imprinted polymer (NIP) demonstrated effective molecular recognition through distinct interfacial changes upon SA rebinding. Detailed EIS/ECS analysis using capacitance and kinetic parameters elucidated the specific binding mechanism versus non-specific effects at the electrochemical interface. Excellent analytical performance is achieved using real capacitance measurements at 0.1 Hz, yielding a linear response to log[SA] (0.25–3.0 ng mL^{-1}) and an ultralow limit of detection (LOD) of 0.02 ng mL^{-1}. Isotherm analysis indicated complex binding involving both specific recognition and non-specific adsorption. The sensor exhibits good selectivity against common interferents, although significant hemoglobin interference is observed at high concentrations. This study validates a robust, highly sensitive, probe-free MIP-capacitance sensor platform suitable for bioanalytical applications requiring trace biomarker quantification.

1. Introduction

Analysis of protein-derived biomarkers has become indispensable in the diagnosis and monitoring of various diseases.[1] These biomarkers are crucial for disease diagnosis, monitoring pathological activity, evaluating treatment efficacy, and understanding therapeutic responses.[2]

Albumin is a promising biomarker because abnormal concentrations in the human body can indicate various conditions, including metabolic disorders, cardiovascular diseases, malnutrition, renal carcinoma, and even viral infections such as SARS-CoV.[3] These diseases often cause changes in albumin concentrations, making it a valuable molecular marker of biological origin.[3] Serum albumin, a globular protein synthesized by hepatocytes in the liver, is the most abundant soluble protein in the circulatory system, playing critical biological, chemical, and pharmacokinetic roles. It is primarily responsible for transporting nutrients, hormones, vitamins, amino acids, mineral salts, and drugs to cells and tissues via the bloodstream. Therefore, monitoring albumin levels is essential for managing metabolic disorders and guiding appropriate clinical treatment.[3] Current analytical methods for albumin detection, such as chemiluminescence,[4] high-performance liquid chromatography,[5] capillary electrophoresis,[6] and immunochemical assay,[7] often rely on sensitivity and selectivity.

H. F. Trevizan, P. C. M. Pizzol, M. F. S. Teixeira
Department of Chemistry and Biochemistry
School of Science and Technology
Sao Paulo State University (UNESP)
Rua Roberto Simonsen, 305, Presidente Prudente, SP 19060-900, Brazil
E-mail: marcos.fs.teixeira@unesp.br

The ORCID identification number(s) for the author(s) of this article can be found under https://doi.org/10.1002/adsr.202500060

DOI: 10.1002/adsr.202500060

A. Olean-Oliveira
Electrochemistry for Energy Conversion
Max Planck Institute for Chemical Energy Conversion
Center for Nanointegration Duisburg-Essen
Duisburg 47057, Germany

P. M. Seraphim
Department of Physiotherapy
School of Science and Technology
Sao Paulo State University (UNESP)
Presidente Prudente, SP, Brazil

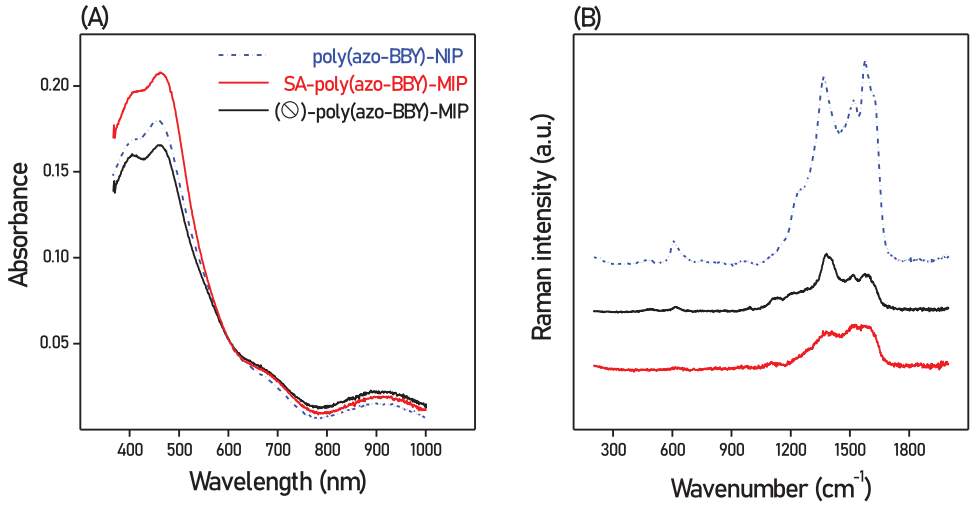

Figure 1. A) UV–vis spectra for poly(azo-BBY)-NIP (blue short dash dot), SA-poly(azo-BBY)-MIP (red line), and (⦸)-poly(azo-BBY)-MIP (black line). B) Raman spectra.

However, these methods can be time-consuming and require expensive equipment and reagents. Consequently, a highly sensitive, rapid, and cost-effective detection platform for albumin identification is highly desirable.

Molecular imprinting technology has attracted significant attention in biomarker detection due to its ability to create sensors with cavities and specific binding sites for target molecules, conferring selectivity and robustness to the sensing platform.[8] Molecularly imprinted polymers (MIPs) are synthetic polymers that mimic biological receptors, exhibiting specificity, sensitivity, and molecular recognition for the target molecule (template).[8,9] The MIP preparation typically involves complexation or pre-polymerization of a functional monomer with the template through van der Waals forces, hydrogen bonds, and Pi-Pi interactions.[10] After the template is incorporated within the polymer matrix, polymerization is initiated, effectively imprinting the target molecules onto the polymer surface. Subsequently, the template is removed, leaving behind template-specific molecular cavities that mimic the shape and functionality of the target molecule.[11] These cavities facilitate rebinding of the target molecule through the same interactions established during the complexation phase. Several recent reviews focused on electrochemical protein-imprinted MIP sensors synthesize advances in functional monomer selection, electropolymerization, synthetic polymer-based imprinting strategies, and performance in clinical matrices.[12] Together, these reviews show that protein-imprinted MIPs mitigate limitations of natural bioreceptors and enable robust label-free and redox-probe-free operation.

Electrochemical techniques, particularly electrochemical capacitance spectroscopy (ECS), have emerged as a sensitive platform for developing and characterizing biomimetic electrochemical sensors.[11] ECS is advantageous for systems based on analyte-molecule interactions, making the fabrication of impedimetric MIP sensors particularly attractive due to their inherent selectivity and sensitivity. In this manuscript, we present a molecularly imprinted polymer-based sensor for the sensitive and selective detection of albumin in biological fluids using electrochemical impedance spectroscopy, without the need for a redox mediator in the analysis solution.

2. Results and Discussion

2.1. Characterization of the Sensor

This section investigates the structural modifications of the poly(azo-BBY) film upon incorporation of the SA template during electropolymerization. **Figure** 1A shows the UV-vis spectra of poly(azo-BBY)-NIP (non-imprinted polymer), SA-poly(azo-BBY)-MIP (imprinted polymer with SA), and (⦸)-poly(azo-BBY)-MIP (imprinted polymer after SA extraction). The spectra of all three films exhibit two absorption bands in the UV region. These bands, located at 403 and 463 nm, are attributed to π-π* and n-π* transitions, respectively, and are indicative of the structural isomerization of the azo polymer.[13] Based on the intensity of the absorption bands, cis-trans isomerism is observed in the macromolecule, with a slight predominance of the cis form.[14,15] This predominance is associated with favorable π-π interactions between the aromatic subunits. The Bismarck Brown Y molecule undergoes trans-cis isomerization during electropolymerization, significantly altering its electronic transition properties.[14] These spectral features suggest a rigid, planar conjugated structure due to strong intramolecular interactions within poly(azo-BBY).[16] The physicochemical properties of the polymer contribute to the formation of the molecular cavity with minimal structural deformation after template extraction. This is evident in the spectra when comparing the absorption peaks of the polymer after target molecule extraction with those of the non-imprinted polymer. Furthermore, no wavelength shift or emergence of a new absorption band is observed.

Subsequently, the same polymers were characterized by Raman scattering spectroscopy (Figure 1B). All Raman spectra show characteristic bands of poly(azo-Bismarck Brown Y) at 1379 cm^{-1} (C—N stretch), 1521 cm^{-1} (C═N stretch), and 1576 cm^{-1} (C═C aromatic stretch). The band at 602 cm^{-1} corresponds to the structural twist of the C—C═N—C bond and the cis-azobenzene

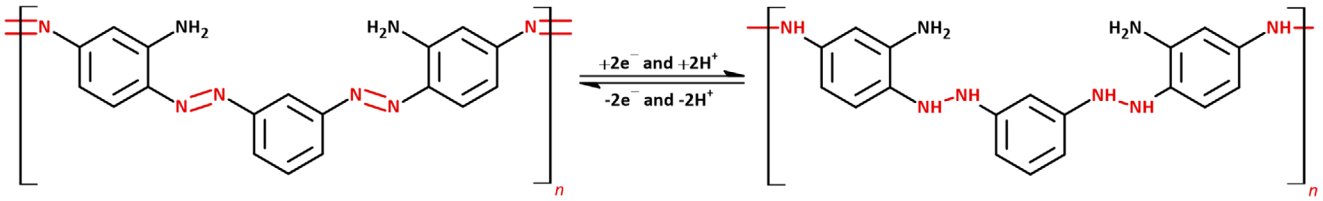

Scheme 1. General redox reaction of the azobenzene moiety in the polymer.

isomer.[17] The primary difference between the spectra is the signal intensity. The relatively weak Raman intensity for SA-poly(azo-BBY)-MIP suggests signal suppression in the deeper layers of the film due to the presence of albumin within the polymer structure. The increased signal for MIP after target molecule removal indicates a greater presence of cavities, facilitating excitation within the polymer.[18] Finally, a peak at 1624 cm^{-1}, observed in all spectra, is associated with the scissoring vibration of the amine group. The low intensity of this band in SA-poly(azo-BBY)-MIP suggests interactions between the template molecule and the polymer structure at the binding site. This decrease in intensity is expected because when the free amino groups of the polymer interact with the SA molecule, their vibrational motion becomes restricted. The scissoring vibration involves the bending of the N—H bonds, and if these bonds are involved in interactions with the SA molecule, their ability to bend freely will be reduced. This leads to a decrease in the intensity of the scissoring vibration band in the Raman spectrum.

2.2. Electrochemical Performance of Device

The electropolymerization profiles for the NIP and MIP films are shown in Figure S1 (Supporting Information). Electropolymerization initiates with the irreversible oxidation of the primary aromatic amines in the BBY monomer, observed at +0.85 V versus SCE in the first potential cycle. In subsequent cycles, the current associated with this initial oxidation decreases as the polymer film grows and passivates the electrode surface, while redox peaks corresponding to the formed azopolymer appear at lower potentials.[19] While the overall shape and peak potentials of the voltammetric profiles are similar for both NIP (Figure S1A, Supporting Information) and MIP (Figure S1B, Supporting Information) synthesis, the current densities observed during MIP formation are noticeably lower than those for the NIP under identical conditions. This suggests that the presence of the bulky SA template molecule in the polymerization solution hinders the diffusion of the BBY monomer to the electrode surface, leading to a slightly slower effective polymerization rate reflected in the lower current. Importantly, the fundamental voltammetric features remain consistent, indicating that SA incorporates into the film without preventing the formation of the poly(azo-BBY) skeleton, consistent with the optical spectroscopic results.

To further characterize the electrochemical impact of template incorporation and removal, the activity of the MIP film with the template retained (SA-poly(azo-BBY)-MIP) was compared to the film after template extraction ((∅)-poly(azo-BBY)-MIP) using cyclic voltammetry (Figure S2, Supporting Information). Both voltammograms display the redox signature characteristic of the poly(azo-BBY) backbone, with broad peaks observed between −0.2 and +0.2 V corresponding to the azo moieties, consistent with previous reports for azopolymers in neutral media.[20] **Scheme 1** represents the oxidation-reduction process of the azobenzene group present in the polymer matrix.[14,19]

However, a noticeable difference is observed in that the peak currents associated with the azo redox process, as well as the overall capacitive currents, are significantly higher for the SA-poly(azo-BBY)-MIP compared to the (∅)-poly(azo-BBY)-MIP after template extraction. This suggests that the presence of the SA template molecule within the polymer matrix may facilitate charge transfer kinetics or enhance the accessibility of the redox sites under these dynamic voltammetric conditions. While this voltammetric behavior indicates enhanced electrochemical activity with the template present, complementary insights into the interfacial resistance and capacitance changes upon template removal, probed under steady-state potential conditions, will be elucidated through the subsequent electrochemical impedance and capacitance spectroscopy analysis.

When the study was performed by impedance spectroscopy (**Figure 2A**), we curiously observed that the capacitive arc of the SA-poly(azo-BBY)-MIP electrode was smaller than that of the (⃠)-poly(azo-BBY)-MIP electrode. EIS studies are usually performed in the presence of a redox probe (e.g., hexacyanoferrate anion)[21] and a concomitant decrease in charge transfer resistance is observed with the formation of cavities generated on the polymer surface. In our case, the EIS study was performed in the absence of the redox probe, and the resistance to charge transfer is related to the azobenzene/hydrazobenzene moieties coupled to protons in the polymer matrix (Scheme 1). The smaller capacitive arc is attributable to the interactions of the polymer sites with the protein structure, essentially the hydrogen bonding interactions with respect to the azo-unit. This is confirmed when we perform the study using the complex capacitance (Figure 2B) in the "redox in" state[22] to determine the redox capacitances. According to Bueno and collaborators,[23] evaluation by capacitance spectroscopy makes it possible to observe the density of the redox state in the molecular layer on the electrode surface. This is verified by the formation of the semicircle in the high to medium frequency range (50 kHz – 56 Hz) in the absence of a diffusion-controlled process. From the complex capacitance results, a decrease in the redox capacitance arc (Figure 2B) is clearly observed after protein desorption on the MIP surface. The redox capacitance changes from 9.5 μF cm^{-2} (SA-poly(azo-BBY)-MIP) to 7.6 μF cm^{-2} ((⃠)-poly(azo-BBY)-MIP).

The impedimetric parameters (**Table 1**) and the equivalent circuit (shown below Table 1) were obtained from the data in Figure 2A.

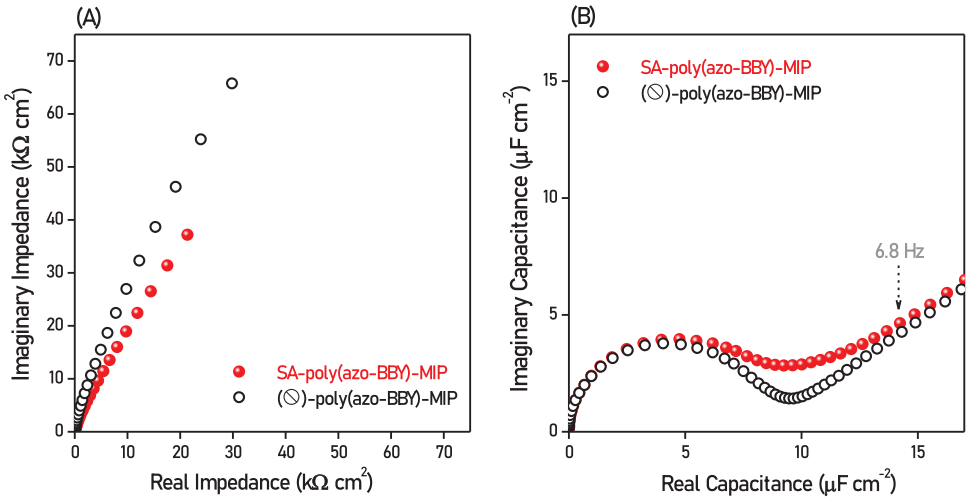

Figure 2. A) Impedimetric Nyquist diagram for SA-poly(azo-BBY)-MIP (red filled circle) and (⦸)-poly(azo-BBY)-MPI (black open circle) in 0.50 mol L^{-1} PBS (pH 7.3) at an applied potential of −0.10 V (vs SCE). B) Nyquist diagram of Imaginary Capacitance versus Real Capacitance in the frequency range 50 kHz to 1.7 Hz. SA-poly(azo-BBY)-MIP (red filled circle) and (⦸)-poly(azo-BBY)-MPI (black open circle) in 0.50 mol L^{-1} PBS (pH 7.3) at an applied potential of −0.10 V (vs SCE).

Table 1. Impedimetric parameters obtained from fitting to the equivalent circuit shown in the footnote below for SA-poly(azo-BBY)-MIP (imprinted polymer with template) and (⦸)-poly(azo-BBY)-MIP (imprinted polymer after template extraction). Measurements were performed in PBS solution (pH 7.4) at −0.10 V (vs SCE) in the absence of dissolved oxygen. R_Ω (solution resistance) = 30 Ω cm^2 for both devices. α_1 and α_2 are the degree of non-ideality of the element.

MIP	R_1	R_2	CPE_1	CPE_2	α_1	α_2
	kΩ cm^2		μF cm^{-2}			
SA-poly(azo-BBY)	63.9	108	26.3	13.3	0.82	0.99
(⦸)-poly(azo-BBY)	10.3	280	16.3	7.19	0.88	0.86

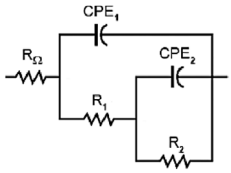

The applicable model for the impedimetric measurements was the adsorption type, which is typical for a signal when the reaction at the electrode is accompanied by an adsorption step or when a large molecule is adsorbed on a porous material.[24] This type of circuit was not expected for the poly(azo-BBY) material, since previously an equivalent circuit composed of three parallel (CPE/R) elements was proposed for a MIP designed for uric acid.[11] That circuit reflected the complexity of the cavities and multiple interfaces formed by the smaller template molecule, allowing the formation of specific recognition sites after extraction. It accounted for electrochemical processes such as charge transfer within the cavities and ion diffusion through the polymer matrix. In contrast, the current work deals with a large template molecule, albumin (7.2 nm diameter), which does not form cavities but rather leaves a "silhouette" or surface imprint on the polymer. The analysis of the impedimetric parameters (Table 1) reveals that the presence of albumin significantly influences the electrochemical behavior of the poly(azo-BBY)-MIP. The decrease in R_1 after albumin extraction is consistent with the removal of a non-conductive barrier at the polymer/solution interface. On the other hand, the dramatic increase in R_2 after albumin extraction can be explained by the role of hydrogen bonding interactions between albumin and the redox-active sites of the polymer. During MIP formation, the acidic environment protonates both the polymer and the template molecule, leading to extensive hydrogen bonding interactions. These interactions are maintained at the interface, facilitating proton transfer and effectively lowering the charge transfer resistance. When albumin is removed, these hydrogen bonding interactions are lost, resulting in a significant increase in R_2. This observation supports the hypothesis that albumin increases the electrochemical activity of the polymer by promoting proton-coupled electron transfer at the redox sites.[32] However, it is important to note that the measurements were performed in a neutral pH solution, where the interaction between the polymer and albumin is likely dominated by other forces, not hydrogen bonding. This aspect will be discussed further when evaluating the sensor performance as a function of albumin concentration. The changes in the CPE values reflect the modification of the polymer surface due to the presence or absence of albumin. The higher CPE_2 value for the SA-poly(azo-BBY)-MIP suggests increased capacitive behavior, likely due to the adsorption of albumin and the resulting changes in the polymer dielectric properties. After extraction, the decrease in CPE_2 indicates a more homogeneous surface with fewer adsorption sites.

To confirm the rebinding of albumin in solution to the imprinted sites on the surface of the (⦸)-poly(azo-BBY)-MIP, EIS/ECS measurements were performed in PBS solution, both in the presence and absence of serum albumin. Parallel measurements were also conducted using a non-imprinted polymer (NIP) of poly(azo-BBY) as a control. The results for the (⦸)-poly(azo-BBY)-MIP and the poly(azo-BBY)-NIP are shown in **Figure** 3A,B. The impedimetric response of the

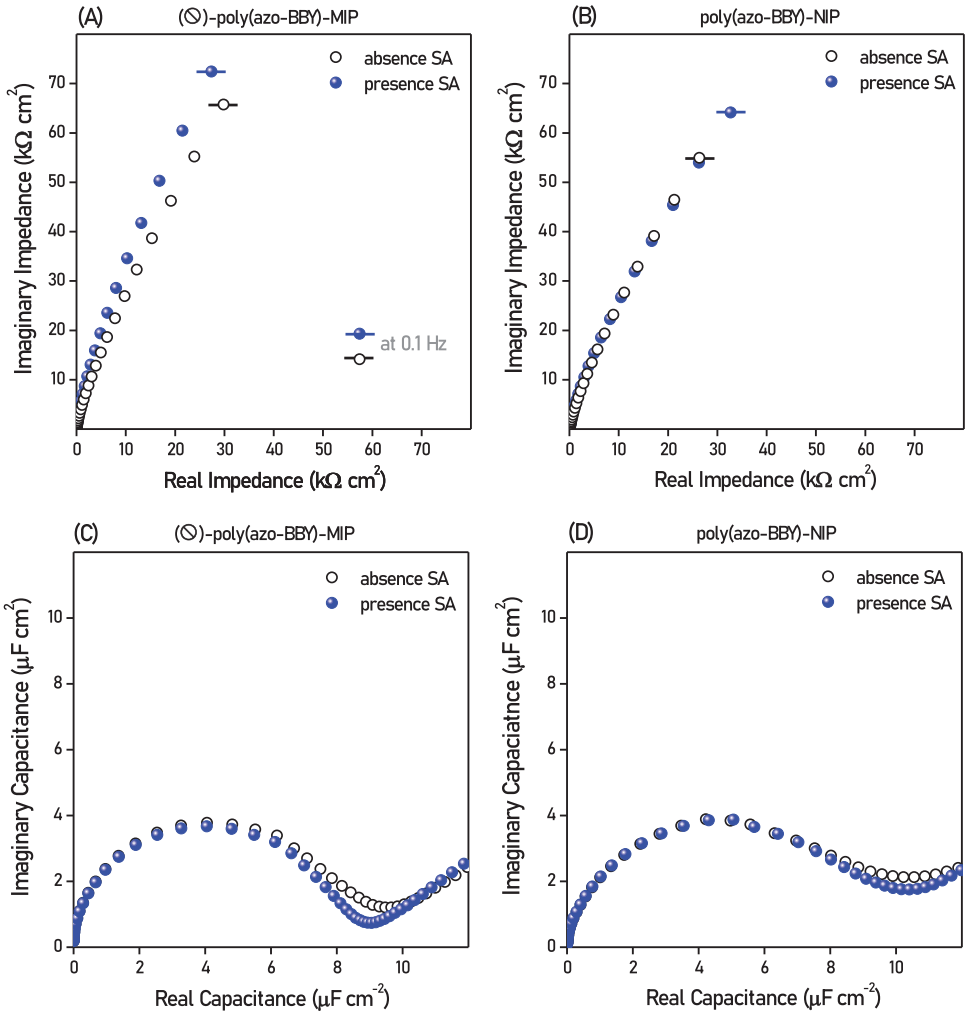

Figure 3. Impedimetric characterization of the (⦸)-poly(azo-BBY)-MIP and poly(azo-BBY)-NIP in the presence and absence of serum albumin (SA). All measurements were performed in 0.50 mol L^{-1} PBS (pH 7.3) at an applied potential of −0.10 V (vs SCE). Black open circles: absence of SA; Blue filled circles: presence of 0.5 ng mL^{-1} SA. A) Nyquist diagram for the (⦸)-poly(azo-BBY)-MIP electrode. B) Nyquist diagrams for the poly(azo-BBY)-NIP electrode. C) Complex capacitance plots (imaginary capacitance versus real capacitance) for the (⦸)-poly(azo-BBY)-MIP electrode. D) Complex capacitance plots (imaginary capacitance versus real capacitance) for the poly(azo-BBY)-NIP electrode.

(⦸)-poly(azo-BBY)-MIP in PBS solution containing 0.5 ng mL^{-1} of SA (Figure 3A) shows an increase in the capacitive arc compared to its response in the absence of SA, indicating increased charge transfer resistance. This behavior is expected since the adsorption of albumin into the imprinted sites on the polymer surface hinders charge transfer. Although the slightly alkaline PBS solution limits hydrogen bonding interactions that could contribute to proton-coupled electron transfer at the polymer redox sites, the high affinity of the imprinted polymer for albumin is evident through other intermolecular interactions, causing a perceptible change in the EIS response.

Conversely, the non-imprinted polymer (Figure 3B) shows no significant change in the capacitive arc upon SA addition. This lack of response confirms that the observed changes in the (⦸)-poly(azo-BBY)-MIP are due to specific interactions between albumin and the imprinted sites, thus demonstrating the successful molecular imprinting of albumin. While the capacitive arc of the poly(azo-BBY)-NIP remains largely unchanged upon the addition of SA, a slight increase in the impedance magnitude is observed at low frequencies (e.g., at 0.1 Hz). This minor difference is likely attributed to weak, non-specific adsorption of albumin onto the polymer surface. Supporting this interpretation, further experiments varying the SA concentration (data not shown) revealed a systematic increase in the low-frequency impedance with increasing albumin concentration. This concentration-dependent behavior is consistent with non-specific adsorption, where a higher concentration of albumin in solution leads to a greater extent of surface coverage, even in the absence of specific binding sites. Although other factors such as alterations in the electrical double layer structure cannot be completely ruled out, the observed concentration dependence strongly suggests that non-specific adsorption is the dominant contributor to the low-frequency impedance changes in the NIP. To quantify the observed changes in the impedance spectra, the data were fitted with the same equivalent circuit as previously.

Table 2. Impedimetric parameters obtained from equivalent circuit fitting (Table 1) for molecularly imprinted polymer (MIP) and the non-imprinted polymer (NIP). Measurements were performed in PBS solution (pH 7.4) at −0.10 V (vs SCE) in the absence and presence of albumin (0.5 ng mL^{-1}) in solution. R_Ω (solution resistance) ≈ 30 Ω cm^2 for both devices. α_1 and α_2 are the degree of non-ideality of the element.

MIP	R_1	R_2	CPE_1	CPE_2	α_1	α_2
	kΩ cm^2		μF cm^{-2}			
Absence SA	10.3	281	16.5	7.20	0.88	0.86
Presence SA	74.6	654	12.1	5.58	0.93	0.78
NIP	**R_1**	**R_2**	**CPE_1**	**CPE_2**	**α_1**	**α_2**
	kΩ cm^2		μF cm^{-2}			
Absence SA	128	207	20.0	9.81	0.86	0.90
Presence SA	124	146	16.5	103	0.88	0.99

As summarized in **Table 2**, the (⦸)-poly(azo-BBY)-MIP exhibits a substantial increase in both R_1 (from 10.3 to 74.6 kΩ cm^2) and R_2 (from 281 to 654 kΩ cm^2) upon the addition of SA. As previously discussed, the increase in R_1 indicates that the binding of albumin hinders charge transport within the polymer film. The significant increase in R_2, the charge transfer resistance at the film/solution interface, warrants further consideration. At the experimental pH of 7.4, extensive hydrogen bonding between the polymer and albumin, as proposed to occur during MIP formation under acidic conditions, is less likely to be the dominant interaction. Instead, other intermolecular forces, such as hydrophobic interactions, van der Waals forces, and potentially electrostatic interactions (depending on the local charge distribution on the albumin and the polymer at this pH), are primarily responsible for the binding of albumin to the imprinted sites.

Crucially, albumin binding, even via non-hydrogen bonding interactions, still significantly impacts the resistance of R_2. This is because the imprinted sites are located on or near the redox-active azobenzene/hydrazobenzene moieties within the polymer. The azobenzene groups are responsible for the electrochemical activity of the polymer, and their redox state is directly linked to charge transfer at the interface. When albumin binds to the imprinted site, it sterically hinders the access of electrolyte ions in solution to these azobenzene groups. This steric hindrance, coupled with any changes in the local microenvironment (e.g., altered local pH or dielectric constant) caused by the bound albumin, directly impedes the electron transfer process associated with the redox cycling of the azobenzene/hydrazobenzene moieties, leading to the observed increase in R_2. The decrease of CPE_1 and CPE_2 values upon SA addition confirm the effect with binding of the bulk molecule. In contrast, the non-imprinted polymer (NIP) shows only minor changes in R_1 and R_2 upon SA addition, consistent with the absence of specific binding sites. However, a significant increase in CPE_2 is observed for the NIP in the presence of SA (from 9.81 to 103 μF cm^{-2}). This increase in CPE_2 suggests non-specific adsorption of albumin onto the NIP surface, leading to changes in the electrical double layer capacitance, as previously discussed.

Building upon the impedance analysis, the complex capacitance response (Figure 3C,D) provides further insights into the interaction between serum albumin (SA) and the molecularly imprinted polymer and the non-imprinted control. The focus here is on the redox capacitance, which is prominent in the high-to-medium frequency range (50 kHz – 21 Hz). Figure 3C shows the complex capacitance response of the (⦸)-poly(azo-BBY)-MIP. In the absence of SA, a distinct arc is observed, representing the redox capacitance associated with the polymer film. Upon the addition of 0.5 ng mL^{-1} SA to the PBS solution, a clear decrease in the magnitude of this redox capacitance arc is observed. This reduction in the arc size directly indicates that SA rebinds to the imprinted sites within the (⦸)-poly(azo-BBY)-MIP. The bound albumin molecules sterically hinder the redox processes occurring within the polymer film, leading to a lower overall capacitance. This is consistent with the increased charge transfer resistance observed in the impedance data (Figure 3A). In contrast, the poly(azo-BBY)-NIP (Figure 3D) exhibits virtually no change in its redox capacitance arc upon the addition of SA. The curves in the presence and absence of SA are nearly superimposable. This confirms that the capacitance change observed in the MIP is a specific consequence of albumin binding to the imprinted cavities, and not a result of non-specific adsorption or bulk solution effects. A key feature to examine is the inflection point between the redox capacitance arc and the transition toward diffusion-influenced capacitance at lower frequencies. In Figure 3C (MIP), this inflection point shifts noticeably upon SA addition. The shift in the inflection to lower imaginary capacitance values (less negative on the y-axis) in the presence of SA corroborates that access to the redox-active sites in the imprinted polymer is being restricted. The albumin, occupying the imprinted cavities, limits the accessibility of these sites to the electrolyte ions, thereby affecting the capacitive behavior. The absence of a significant shift in this inflection point for the NIP (Figure 3D) further reinforces the specificity of the interaction with the MIP. The reduction of redox capacitance arc, added to shift in the inflection for the MIP can be associated to the occupation of SA in the redox-active sites.

Bode diagrams of the imaginary capacitance versus the logarithm of frequency (Figure S3, Supporting Information) provide further insights into the SA-polymer interactions, highlighting the frequency-dependent capacitive behavior and allowing the determination of the relaxation time constant (τ_r). Comparing MIP (Figure S3A, Supporting Information) and NIP (Figure S3B, Supporting Information) in the absence of SA, the NIP exhibits a significantly longer τ_r (0.58 ms) than the MIP (0.28 ms), reflecting the MIP more structured environment due to imprinting, which facilitates faster charge transport and redox processes. Upon SA addition, the MIP relaxation time remains essentially unchanged, confirming that while the extent of the redox process diminishes (see Figure 3C), the rate is not significantly affected by SA rebinding. This is consistent with SA primarily blocking access to redox sites rather than altering the redox kinetics. In contrast, the NIP shows a substantial increase in τ_r upon SA addition (from 0.58 ms to 0.74 ms), supporting non-specific albumin adsorption, which hinders ion movement and slows interfacial processes. The The NIP relaxation time becoming longer than the MIP with SA present highlights the impact of this non-specific adsorption.

Following Bueno and Davis,[25] the electron transfer rate constant (k_r) is inversely proportional to the relaxation time ($k_r = 1/\tau_r$). Thus, the MIP shorter relaxation time without SA corresponds to a faster electron transfer rate ($k_r = 3.57\ ms^{-1}$) compared to the NIP ($k_r = 1.72\ ms^{-1}$), consistent with the MIP more or-

dered structure promoting better electronic coupling between the redox-active azobenzene/hydrazobenzene moieties and the electrode. SA rebinding to the MIP does not affect k_r of the remaining accessible sites, while SA addition to the NIP decreases k_r, consistent with hindered electron transfer. Concluding this study, the full width at half maximum (FWHM) of the imaginary capacitance peaks provides information about the kinetic dispersion of the redox processes. A larger FWHM indicates a broader distribution of relaxation times, suggesting greater heterogeneity in the electron transfer kinetics. The FWHM was found to be 1.376 for the (⦸)-poly(azo-BBY)-MIP and significantly larger, at 1.966, for the poly(azo-BBY)-NIP (Figure S3A,B, Supporting Information). This result clearly indicates that the MIP exhibits lower kinetic dispersion than the NIP. The narrower peak for the MIP suggests a more homogeneous environment for electron transfer, consistent with its more ordered structure. Conversely, the broader peak for the NIP (larger FWHM) indicates greater kinetic dispersion, as expected for a non-imprinted polymer lacking defined binding sites. The addition of SA does not significantly change the peak width and FWHM.

2.3. Analytical Performance of Molecularly Imprinted Polymer Device

Figure 4 illustrates the analytical performance of the (⦸)-poly(azo-BBY)-MIP sensor evaluated toward varying concentrations of SA biological marker using EIS, particularly in the medium-to-low frequency region. To ensure the reliability and sensitivity of the technique, these measurements were performed in triplicate using three independently prepared sensors. The changes in complex capacitance (Figure 4A), real capacitance (Figure 4C), and imaginary capacitance (Figure 4E) were monitored across the concentration range (0.0 to 3.0 ng mL^{-1}). All three capacitance parameters derived from the EIS measurements exhibit a clear dependence on the SA concentration. As the SA concentration increases, the redox capacitance arc decreases, and both the real and imaginary capacitance values decrease, particularly at lower frequencies. This behavior indicates progressive filling of the imprinted cavities and loading of the molecular film surface as more SA molecules bind. The overall trend across all parameters suggests a surface saturation process, consistent with an adsorption isotherm model, which is expected for a sensor based on specific binding sites reaching their capacity.

The analytical curve derived directly from the redox capacitance (C_{redox}) and plotted against linear SA concentration (Figure 4B) clearly shows a decrease as [SA] increases. However, this relationship is notably non-linear over the full concentration range, exhibiting the characteristic curvature associated with surface saturation. Closer inspection suggests the presence of potentially two distinct linear response regions within this curve. While attempts could be made to linearize segments of this response, potentially through logarithmic transformation of the concentration (as often done for isotherms), the primary plot in Figure 4B highlights the direct, albeit non-linear, relationship. Equations 1 and 2 likely represent linear fit derived from such an approach or describes the response within one of the specific linear segments observed. Conversely, when plotting the real capacitance (Figure 4D) and imaginary capacitance (Figure 4F) — extracted at a fixed low frequency of 0.10 Hz — against the logarithm of SA concentration, well-defined linear relationships were obtained across the tested range. This linearization using the logarithm of the concentration is typical for sensor responses that span several orders of magnitude or follow binding isotherms. Both Real and Imaginary capacitances decrease linearly with increasing log[SA], with these linear responses being accurately described by Equations (3) and (4), respectively.

$$C_{redox}\left(\mu Fcm^{-2}\right) = 9.812 - 0.479\left[SA\left(ngmL^{-1}\right)\right] \quad r = 0.9987 \quad \left(\text{interval } 0.25 - 1.0\ \text{ngmL}^{-1}\right) \tag{1}$$

$$C_{redox}\left(\mu Fcm^{-2}\right) = 9.534 - 0.209\left[SA\left(ngmL^{-1}\right)\right] \quad r = 0.9997 \quad \left(\text{interval } 0.25 - 3.0\ \text{ngmL}^{-1}\right) \tag{2}$$

$$C_{real}\left(\mu Fcm^{-2}\right) = 10.664 - 1.008\log\left[SA\left(ngmL^{-1}\right)\right] \quad r = 0.9978 \quad \left(\text{interval } 0.25 - 3.0\ \text{ngmL}^{-1}\right) \tag{3}$$

$$C_{imag}\left(\mu Fcm^{-2}\right) = 1.131 - 0.315\log\left[SA\left(ngmL^{-1}\right)\right] \quad r = 0.9983 \quad \left(\text{interval } 0.25 - 3.0\ \text{ngmL}^{-1}\right) \tag{4}$$

Comparing the sensitivities, determined from the slopes of the linear calibration curves, it is evident that the real capacitance measured at 0.10 Hz provides the highest sensitivity (steeper slope) to changes in SA concentration within this range. Therefore, while monitoring C_{redox} offers a direct visualization of the binding in the complex plane, analyzing the real capacitance component at a low, fixed frequency appears to be the most sensitive and practical approach for quantitative SA determination using this MIP sensor, offering a robust linear calibration.

Since the real capacitance provided the highest sensitivity for SA detection, the limit of detection (LOD) for the MIP sensor was determined using this parameter. Due to the inherent sigmoidal relationship typically observed between sensor response and analyte concentration in binding-based assays reflecting surface saturation, the LOD was calculated by fitting a four-parameter logistic (4PL) equation[26] to the real capacitance data (plotted against linear SA concentration) via non-linear regression analysis using OriginPro software.[26] This model accurately describes the sensor response curve, particularly in the low concentration range crucial for LOD determination. It is important to note that the standard LOD calculation method (3s/slope) could not be reliably applied directly to the linearized plot shown previously (Figure 4D). The resulting fitted curve and the 4PL equation obtained from the real capacitance values as a function of SA concentration are presented in the supplementary material (Figure S4; Equation S1, Supporting Information). Based on the four-parameter logistic (4PL) model fitted to the real capacitance data, the limit of detection (LOD) for SA was calculated to be 0.02 ng mL^{-1}. Comparison with recent electrochemical MIP sensors for SA (**Table 3**) shows that the present probe-free, real-capacitance device delivers low-ng mL^{-1} sensitivity with a working range of 0.25–3.0 ng mL^{-1}. Relative to semi-covalent polythiophene MIPs

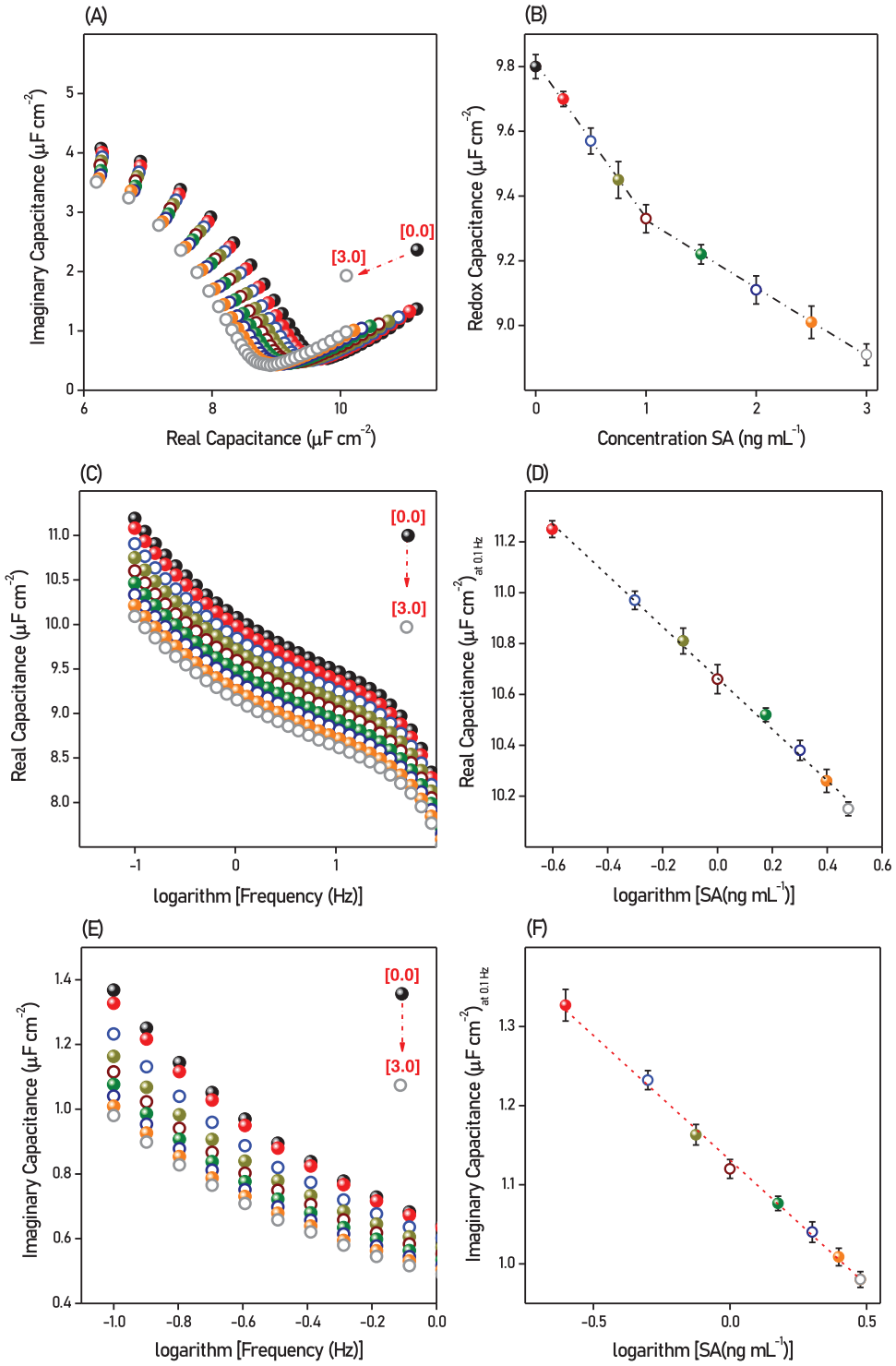

Figure 4. Analytical performance of the MIP sensor for serum albumin (SA) detection. Measurements were performed in PBS (pH 7.4) at −0.10 V (vs SCE) with varying SA concentrations (ranging from 0.0 to 3.0 ng mL^{-1}). Error bars represent the standard deviation from three independent sensor measurements (n = 3). A) Complex capacitance plots showing the decrease in the redox capacitance arc with increasing SA concentration. The arrows indicate the trend from 0.0 ng mL^{-1} (black circle) to 3.0 ng mL^{-1} (gray open circle). B) Analytical curve obtained from the C_{redox} versus SA concentration. C) Bode plots showing the real capacitance (C′) response versus log(frequency) for different SA concentrations. D) Analytical curve obtained from the C′ extracted at 0.1 Hz versus log(SA concentration). E) Bode plots showing the imaginary capacitance (C″) response versus log(frequency) for different SA concentrations. F) Analytical curve obtained from the C″ extracted at 0.10 Hz versus log(SA concentration).

Table 3. Recent electrochemical MIP sensors for human serum albumin (HSA).

Sensing platform (recognition)	Electrochemical readout	Linear range	LOD (ng mL^{-1})	Reference
poly(azo-BBY)	Probe-free real capacitance (EIS)	0.25–3.0 ng mL^{-1}	0.02	This work
Semi-covalent polythiophene	DPV (ferri/ferrocyanide)	0.8–20 µg mL^{-1}	16.6	[27]
Semi-covalent polythiophene	EIS (ferri/ferrocyanide)	4–80 µg mL^{-1}	800	[27]
AuNPs/PTH–MB	Dual DPV + EIS	0.1–100,000 ng L^{-1}	3.0×10^{-5}	[28]
Polyscopoletin nanofilm	CV (ferri/ferrocyanide)	20–100 mg L^{-1}	3700	[29]
PoPD layers	SWV (Fc)	5–100 ng mL^{-1}	1.5	[30]

Abbreviations: **AuNPs** = gold nanoparticles; **EIS** = electrochemical impedance spectroscopy; **DPV** = differential pulse voltammetry; **CV** = cyclic voltammetry; **SWV** = square-wave voltammetry; **PTH–MB** = poly(thionine–methylene blue); **PoPD** = Poly(o-phenylenedia**Fc** = ferrocene;

on Au (DPV LOD = 16.6 ng mL^{-1}; EIS LOD = 800 ng mL^{-1}) and to the polyscopoletin MIP nanofilm (CV LOD = 3.7 mg L^{-1}), our sensor is 2–5 orders of magnitude more sensitive, while avoiding external redox probes. A DPV/EIS architecture that embeds electroactive layers (AuNPs/poly(thionine–methylene blue)) reports an ultra-low LOD (0.03 ng L^{-1}); however, it relies on dual-signal amplification and mediator-dependent readout, whereas our platform attains nanogram-per-milliliter detection without redox mediators, using a single, label-free capacitance metric. For broader context beyond MIPs, Supplementary Table S1 (Supporting Information) compiles other transduction strategies applied to SA determination.

The binding affinity and mechanism of albumin interaction with the (⦸)-poly(azo-BBY)-MIP were investigated by fitting the experimental data, derived from redox capacitance changes (ΔC_{redox}), to various isotherm models using linearized plots (**Figure 5**). Redox capacitance was chosen as the response parameter as it is closely related to the binding events at the imprinted sites.[31] Analysis using the linearized Langmuir plot (Figure 5A) showed a strong linear correlation (r = 0.9948) across the concentration range presented in this form. This indicates that the Langmuir model, assuming monolayer adsorption onto a finite number of homogeneous sites, provides a good mathematical description of the binding data. This fit allows the estimation of Langmuir parameters, consistent with the presence of specific, saturable binding sites created during imprinting (K_L = 0.240 ng mL^{-1}).

However, plotting the data according to the linearized Freundlich model (Figure 5B) provides crucial insights into the complexity of the interaction. This plot clearly exhibits a change in slope, indicating that the binding mechanism cannot be described by a single Freundlich relationship across the entire concentration range, with a distinct transition point occurring around ln[SA] ≈ 0. Although the Freundlich affinity constants (K_F) were numerically similar for both regimes (0.481 vs 0.465, obtained from intercepts in Figure 5B), the distinct difference in the exponents (n_1 vs n_2) clearly highlights the fundamentally different adsorption energetics governing the two concentration ranges. At lower concentrations (ln[SA] < 0), the slope ($1/n_1$ = 1.118 with r = 0.9991) is steep and greater than 1, while at higher concentrations the slope ($1/n_2$ = 0.581 with r = 0.9990) becomes significantly shallower and is less than 1.

This breakpoint supports a dual-regime binding mechanism: an initial regime dominated by high-affinity binding to imprinted sites, followed by a regime in which lower-affinity, heterogeneous interactions prevail as concentration increases and non-specific adsorption becomes relevant on the polymer surface after saturation of the primary sites. At high SA concentrations, the residual increase in signal outside the specific-binding regime is attributed to non-specific adsorption driven mainly by hydrophobic and π–π contacts between the azo/aromatic polymer matrix and hydrophobic/π-rich patches on SA, complemented by hydrogen bonding and patchy electrostatic interactions. As the high-affinity imprinted cavities saturate, mass action promotes occupancy of shallower or less-defined sites and adsorption on heterogeneous surface domains, giving rise to the shallower second slope in the calibration. The poly(azo-BBY) layer exhibits heterogeneity in site depth, cross-link density, and local porosity, which imparts a distribution of binding energies; accordingly, the data are well rationalized by two-regime (bi-Langmuir) or Langmuir–Freundlich (n < 1) descriptions rather than a single-site model. A global Sips (Langmuir–Freundlich) fit describes the full concentration range well (Figure 5C), with linearity. This indicates that the Sips model, which incorporates surface heterogeneity, can effectively describe the overall binding behavior across the concentration range studied. The Sips fit yields parameters (K_{LF} = 0.755, 1/n ≈ 1.20) reflecting this averaged heterogeneity (n ≠ 1). The heterogeneity factor 1/n > 1 aligns with the concept of a non-ideal surface created by the imprinting process.

Molecular recognition and selectivity are crucial parameters for evaluating the effectiveness of the sensor imprinting process. Selectivity was evaluated against potentially interfering species commonly found in biological fluids, including hemoglobin (Hb), glucose oxidase (GOx), glucose (Glu), L-histidine (His), L-tyrosine (Tyr), L-cysteine (Cys), tryptophan (Trp), L-ornithine (Orn), bovine serum albumin (BSA), and urea. To test the sensor selectivity, the (⦸)-poly(azo-BBY)-MIP electrode response was measured in the presence of these interferents at a concentration 1000 times greater than that of a reference SA concentration (0.5 ng mL^{-1}). Changes were monitored using the redox capacitance values. The relative interference was calculated as the percentage change relative to the SA signal: $[(S_i / S_{SA}) - 1] \times 100\%$, where S_i is the signal in the presence of the interferent and S_{SA} is the signal for SA alone. **Figure 6** presents the results of these selectivity studies. The device demonstrated excellent selectivity, showing interference values below 5% for common clinical analytes such as glucose, various amino acids

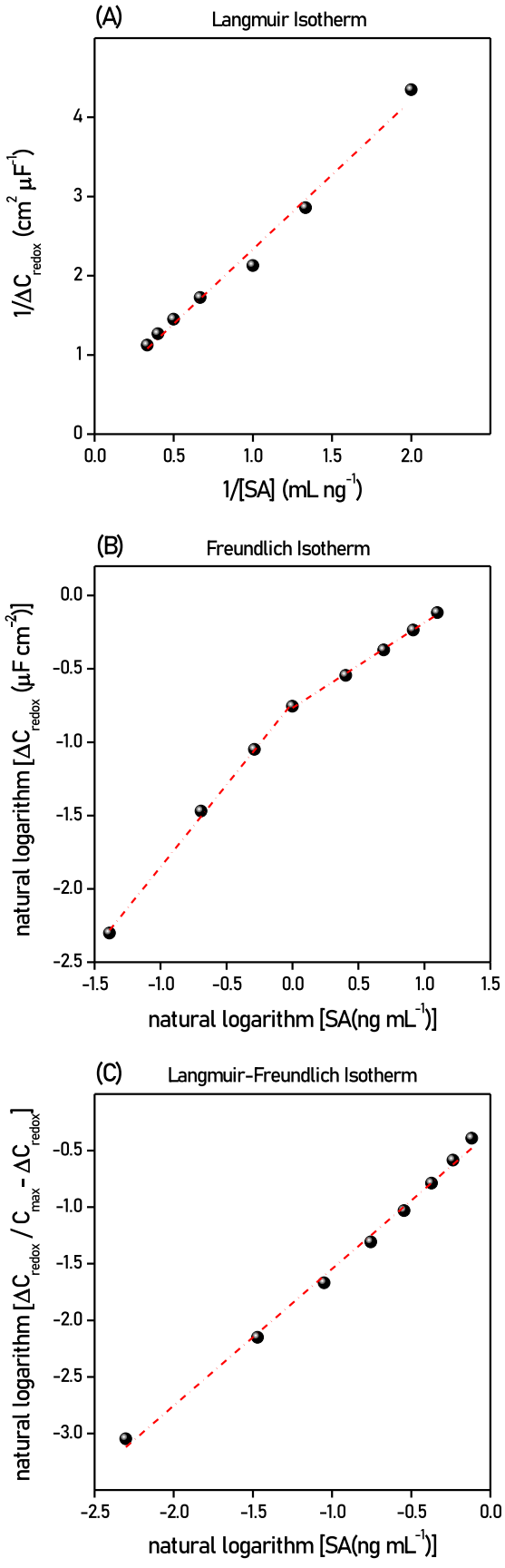

(His, Tyr, Cys, Trp, Orn), urea, and the enzyme glucose oxidase, even at these high interferent concentrations. Bovine serum albumin (BSA), which is structurally similar to SA, showed only moderate interference of 8%. This relatively low cross-reactivity with BSA highlights the effectiveness of the imprinting process in creating specific recognition sites tailored to SA, likely involving interactions with functional groups distinguishing the target molecule. However, significant interference, exceeding 15%, was observed for hemoglobin (Hb). This level of interference was anticipated and can likely be attributed to potential charge transfer interactions occurring between the redox-active poly(azo-BBY) film and the heme group within hemoglobin, particularly at the high relative concentration tested (1000-fold excess). In practical use, interference can be minimized by sample dilution (to reduce [Hb]:[SA] ratio) and, if needed, by a brief off-sensor selective extraction/enrichment of SA prior to measurement.

The device showed interference values below 5% for molecules that are common in clinical analysis such as glucose, amino acids, urea and the enzyme glucose oxidase. Bovine-derived albumin (BSA) has been shown to perturb the total system response by an 8% interference. The BSA and SA molecules, despite being structurally similar, the complexation step in the construction of the sensor proved to be effective in forming specific interactions with functional groups existing only in the SA molecule. However, for hemoglobin the interference values were significant, above 15%. Such interference was already expected, since both Hb and SA molecules have adsorption properties and occupation of active sites present at the polymer/solution interface. Therefore, it was possible to conclude that the sensor is selective for most molecules studied. The formation of specific cavities for SA has been proven when compared to the BSA molecule that has similar structures.

Finally, the reproducibility and stability of the (⦸)-poly(azo-BBY)-MIP sensor were evaluated to assess its practical viability (**Figure** 7). Both parameters were investigated by monitoring the real capacitance signal after incubating the sensors in a 0.5 ng mL^{-1} SA solution to facilitate analyte rebinding. To assess fabrication reproducibility, seven independently prepared MIP sensors were tested at the same analyte level and their responses were normalized to the batch average (set to 100%). As shown in Figure 7A, the relative responses clustered around unity (90–112%), yielding a relative standard deviation (RSD) of 8.98%, which indicates good between-sensor reproducibility for this fabrication route. The response of a single sensor monitored over 14 days (normalized to day 1 = 100%) showed low day-to-day variability (RSD 9.56%) (Figure 7B). While a modest upward drift is observed at later time points, no loss of activity occurred, indicating preserved sensing capability over two weeks.

Figure 5. Isotherm analysis of SA binding to the (⦸)-poly(azo-BBY)-MIP using redox capacitance changes (ΔC_{redox}) derived from ECS measurements. Linearized plots for: A) Langmuir isotherm (1/ ΔC_{redox} vs 1/[SA]), B) Freundlich isotherm (ln(ΔC_{redox}) vs ln[SA]), and C) Langmuir-Freundlich (Sips) isotherm (ln[ΔC_{redox} / (ΔC_{max})] vs ln[SA]). Data points represent experimental measurements, and dashed lines show the linear fits used to extract isotherm parameters. The ΔC_{max} value used in (C) was obtained from non-linear Langmuir fitting of the original data.

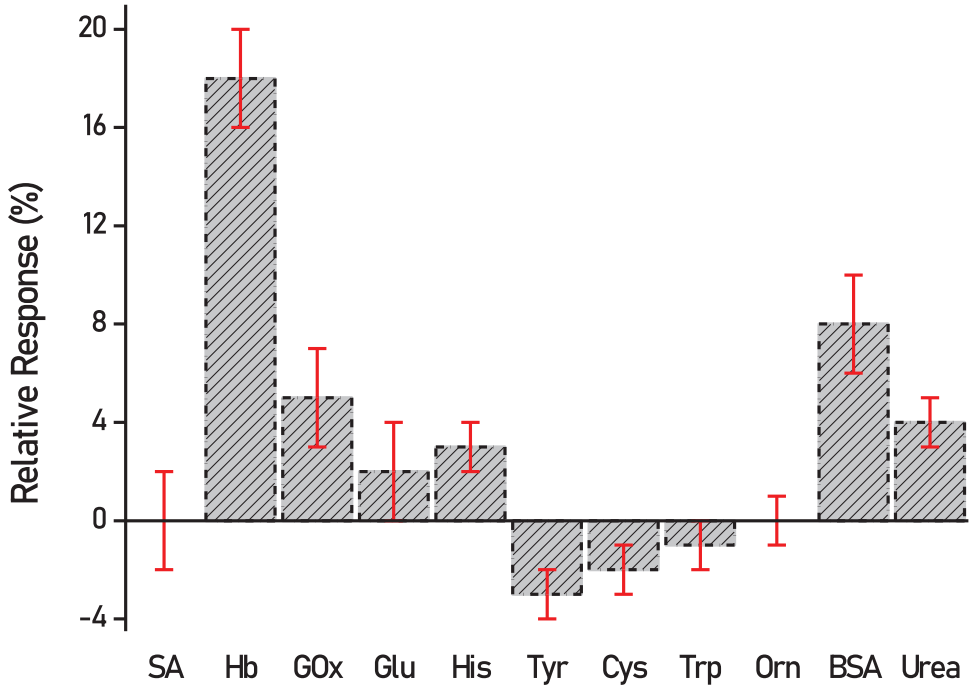

Figure 6. Selectivity of the (⦸)-poly(azo-BBY)-MIP sensor. Interferent concentration was 1000-fold higher than the SA concentration (0.5 ng mL^{-1}). Relative response calculated from redox capacitance changes. Measurements performed in PBS (pH 7.3) at −0.10 V (vs SCE). Error bars represent the standard deviation from three independent sensor measurements (n = 3).

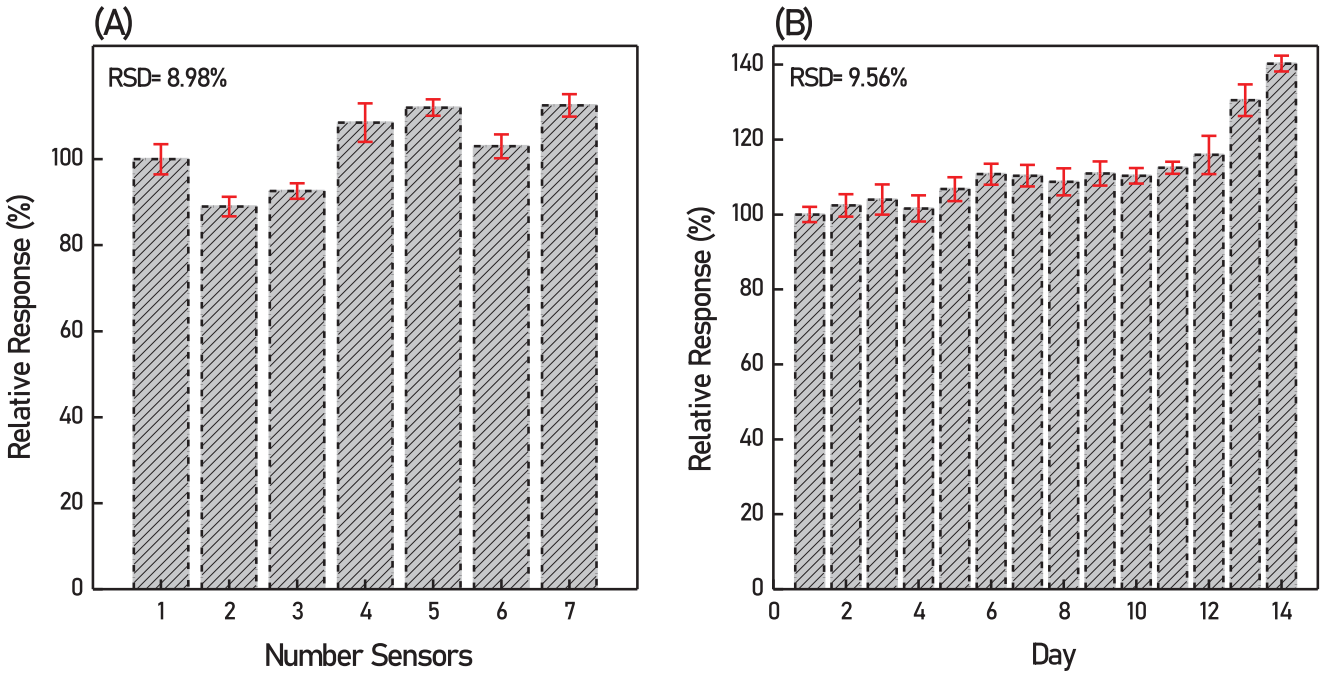

Figure 7. Reproducibility and short-term stability of the (⦸)-poly(azo-BBY) MIP sensor. A) Relative response (%) for seven independently fabricated sensors (each electropolymerized on a different FTO substrate) measured after incubation in 0.5 ng mL^{-1} SA; values normalized to the batch average (100%). RSD = 8.98%. B) Relative response of a single sensor monitored over 14 days under the same conditions, normalized to day 1 (100%); the sensor was refrigerated in buffer between measurements. RSD = 9.56%. Error bars denote standard deviation of replicate readings. In both panels, bars show mean ± SD of triplicate measurements (n = 3 per bar).

3. Conclusion

In this work, a novel electrochemical sensor based on a molecularly imprinted polymer was successfully developed and characterized for the sensitive detection of human serum albumin (SA) without the need for external redox probes. Comparative studies using EIS and ECS definitively demonstrated the sensor specific molecular recognition capabilities. The rebinding of SA to the MIP resulted in significant increases in charge transfer resistance and corresponding decreases in capacitance parameters, consistent with the specific occupation of imprinted sites near the polymer active sites. In contrast, the non-imprinted polymer (NIP) exhibited negligible specific response, primarily showing signs of non-specific adsorption at low frequencies and in the double-layer capacitance. Detailed analysis of relaxation times (τ) and kinetic dispersion (FWHM) further elucidated the binding mechanisms, showing faster intrinsic kinetics for the MIP and confirming that SA binding primarily blocks access to sites rather than altering intrinsic rates, while non-specific adsorption slowed kinetics on the NIP. While redox capacitance offered direct insight into binding, the real capacitance (C') measured at a low frequency (0.10 Hz) provided the highest sensitivity, yielding a linear calibration curve against log[SA] in the range of 0.25–3.0 ng mL^{-1}. A limit of detection (LOD) of 0.02 ng mL^{-1} was achieved using a 4PL model fit, demonstrating superior sensitivity compared to several previously reported SA sensors. The achieved low detection limit highlights the potential of this approach for bioanalytical applications requiring trace-level quantification of albumin and other relevant protein biomarkers. Isotherm analysis revealed a dual-regime binding mechanism, initiated by specific Langmuir-type interactions at low concentrations, followed by Freundlich-type non-specific adsorption at higher concentrations, with the Sips model effectively describing the overall heterogeneous binding. The sensor displayed good selectivity against common physiological interferents, although significant interference from hemoglobin at high concentrations suggests potential charge transfer interactions.

4. Experimental Section

Chemicals: Hydrochloric acid (≥99%), potassium chloride (≥99%), Bismarck Brown Y (BBY, ≥90%), serum albumin (SA ≥99%), potassium dihydrogen phosphate (≥99%), dipotassium hydrogen phosphate (≥99%), hemoglobin (Hb ≥99,9%), *glucose oxidase* (GOx ≥99.9%), glucose (Glu ≥ 99.9%), urea (≥99.9%), serum albumin (SA≥ 99.9%), L-histidine (His ≥99.9%), L-Cysteine (Cys ≥99.9%), L-ornithine (Orn ≥99.9%), L-tyrosine (Tyr ≥99.9%) and tryptophan (Trp ≥99.9%) were purchased from Merck and Sigma-Aldrich. Gaseous nitrogen (N_2, ≥99.8%) was purchased from White Martins.

Materials: All electrochemical measurements were performed in a conventional three-electrode electrochemical cell. The working electrode was a fluoride-doped tin oxide (FTO) electrode (1.0 cm^2), modified with the molecularly imprinted polymer (MIP-electrode, 1.0 cm^2). A platinum (Pt) electrode served as the counter electrode, and a saturated calomel electrode (SCE) was used as the reference electrode.

Preparation of Molecularly Imprinted Polymer-Based Sensor: The poly(azo-BBY)-MIP was electrosynthesized using cyclic voltammetry in a potential range of -0.30 to +1.0 V *versus* SCE. The electropolymerization solution, consisting of 10.0 mmol L^{-1} BBY monomer and 0.5 ng mL^{-1} serum albumin (SA) as the template molecule in 0.50 mol L^{-1} KCl (pH 2.0), was deoxygenated by bubbling with nitrogen gas. During the electropolymerization process, a nitrogen atmosphere was maintained over the solution. The poly(azo-BBY)-MIP sensing platform was prepared using this optimized solution.[11] The electropolymerization solution consisted of 10.0 mmol L^{-1} BBY monomer and 0.5 ng mL^{-1} SA as the template molecule in 0.50 mol L^{-1} KCl (pH 2.0). Electropolymerization was carried out over 20 potential sweep cycles at a scan rate of 20 mV s^{-1}. After fabrication, the MIP electrode was thoroughly rinsed with deionized water to remove any surface residues. To extract the SA template from the polymer matrix, the MIP electrode was immersed in phosphate buffer for 30 min and subjected to potential scans in the range from -0.30 to+1.0 V *versus* SCE at a scan rate of 50 mV s^{-1}. This extraction process was continued until the current magnitude stabilized over successive potential cycles.

For comparison, a non-imprinted polymer (NIP) film was synthesized using the same procedure but without the addition of the SA template. The electrodes were designated as follows: poly(azo-BBY)-NIP (non-imprinted), SA-poly(azo-BBY)-MIP (imprinted with template), and (⦸)-poly(azo-BBY)-MIP (imprinted after template extraction).

Electrochemical Study of the MIP Sensor: All electrochemical measurements were performed using a PalmSens3 potentiostat controlled by PStrace 5.8 software, with both the MIP and NIP films. The electrochemical behavior of the poly(azo-BBY)-MIP films was investigated in 0.10 mol L^{-1} phosphate-buffered saline (pH 7.3) in the absence and presence of 0.5 ng mL^{-1} SA using electrochemical impedance spectroscopy (EIS). EIS/ECS measurements were conducted over a frequency range of 50 kHz to 0.1 Hz, with 10 points per decade, at an applied potential of −0.10 V *versus* SCE using the three-electrode system. All impedance spectra were modeled using the EIS Spectrum Analyzer software to extract the equivalent circuit and the corresponding electrochemical parameters. The errors presented for the mathematical adjustments were less than 5%.

Optical Characterization of the MIP Sensor: UV–vis spectroscopy was performed using a Varian Cary 50 spectrophotometer (350-1000 nm). Absorption spectra of the BBY and BBY-SA films electropolymerized on FTO were acquired by placing the electrodes in the instrument optical path. Raman scattering measurements were performed using a Renishaw inVia microRaman spectrograph coupled to a Leica optical microscope with a 50X objective lens. A 514.5 nm excitation laser with an 1800 lines mm^{-1} diffraction grating and a spectral resolution of 4 cm^{-1} was used. Raman spectra were collected for the MIP films (before and after SA extraction) and the NIP film on the FTO substrate to investigate potential interactions between SA and the poly(azo-BBY)-MIP polymer/cavities.

Statistical Analysis: All electrochemical measurements related to the analytical performance, selectivity, reproducibility, and stability of the sensor were performed in triplicate (n = 3) using independently prepared sensors. Data are presented as mean ± standard deviation (SD), with the standard deviation represented by error bars in the figures. For the analytical curves, a logarithmic transformation of the serum albumin (SA) concentration was performed to establish a linear relationship with the real and imaginary capacitance responses. These relationships were analyzed using linear regression, and the quality of the fit was determined by the correlation coefficient (r). The limit of detection (LOD) was fitted to the data using a non-linear regression analysis with a four-parameter logistic (4PL) model. All data processing, statistical analysis, curve fitting (linear and non-linear), and graph plotting were performed using the OriginPro 8.5 software.

Supporting Information

Supporting Information is available from the Wiley Online Library or from the author.

Acknowledgements

The authors gratefully acknowledge the crucial financial support from CEPID-FAPESP (2013/07296-2) and CNPq (308232/2023-2). H.F.T. and M.L.P. gratefully acknowledge CAPES (88887.831630/2023-00) for their master's scholarships. The authors thank the Gemini language model for assistance in improving the clarity and readability of this manuscript. SJT.

Conflict of Interest

The authors declare no conflict of interest.

Author Contributions

H.F.T. performed investigation, visualization, discussion, and wrote original draft. P.C.M.P. performed data discussion. A.O.-O. performed conceptualization, data discussion. P.M.S. performed visualization, discussion, funding acquisition, and reagent suppliers. M.F.S.T. performed conceptualization, methodology, validation, wrote – Review and Edited, supervision, project administration, and funding acquisition. SJT Δ

Data Availability Statement

The data that support the findings of this study are available from the corresponding author upon reasonable request.

Keywords

capacitance sensor, human serum albumin, molecular recognition, molecularly imprinted polymer, probe-free detection

Received: April 10, 2025
Revised: September 2, 2025
Published online: September 25, 2025

[1] a) B. Jin, A. M. Huang, R. B. Zhong, B. H. Han, *Chemotherapy* **2010**, *56*, 417; b) H. S. Kim, T. Lee, J. Yun, G. Lee, Y. Hong, *Microchem. J.* **2021**, *160*, 105632.
[2] a) S. Bolisetty, A. Agarwal, *Am J Physiol-Renal* **2011**, *300*, F626; b) N. Rifai, M. A. Gillette, S. A. Carr, *Nat. Biotechnol.* **2006**, *24*, 971.
[3] a) G. H. Tesch, *Nephrology* **2010**, *15*, 609; b) H. J. Lambers Heerspink, J. W. Brinkman, S. J. L. Bakker, R. T. Gansevoort, D. de Zeeuw, *Curr Opin Nephrol Hy* **2006**, *15*, 631; c) P. Paliogiannis, A. A. Mangoni, M. Cangemi, A. G. Fois, C. Carru, A. Zinellu, *Clin Exp Med* **2021**, *21*, 343; d) E. Gremese, D. Bruno, V. Varriano, S. Perniola, L. Petricca, G. Ferraccioli, *J Clin Med* **2023**, *12*, 6017.
[4] a) S. Aoyagi, T. Iwata, T. Miyasaka, K. Sakai, *Anal. Chim. Acta* **2001**, *436*, 103; b) J. Kang, J. M. Shen, Z. L. Chen, J. Nan, X. Huang, L. Han, W. P. Hao, *RSC Adv.* **2015**, *5*, 89569.
[5] C. Boiero, D. Allemandi, M. Longhi, J. M. Llabot, *J Pharmaceut Biomed* **2015**, *111*, 186.
[6] H. B. Duan, J. T. Cao, J. J. Yang, H. Wang, Y. M. Liu, *Talanta* **2016**, *154*, 341.
[7] a) J. W. Keyser, R. Fifield, G. L. Watkins, *Clin. Chem.* **1981**, *27*, 736; b) G. P. Dooley, W. H. Hanneman, D. L. Carbone, M. E. Legare, M. E. Andersen, J. D. Tessari, *Chem. Res. Toxicol.* **2007**, *20*, 1061.
[8] M. Parlapiano, Ç. Akyol, A. Foglia, M. Pisani, P. Astolfi, A. L. Eusebi, F. Fatone, *J. Environ. Chem. Eng.* **2021**, *9*, 105051.
[9] X. Wang, Y. Y. Wang, X. X. Ye, T. Wu, H. P. Deng, P. Wu, C. Y. Li, *Biosens. Bioelectron.* **2018**, *99*, 34.
[10] a) A. M. Mostafa, S. J. Barton, S. P. Wren, J. Barker, *Trac-Trend Anal Chem* **2021**, *144*, 116431; b) B. Fresco-Cala, A. D. Batista, S. Cárdenas, *Molecules* **2020**, *25*, 4740.
[11] H. F. Trevizan, A. Olean-Oliveira, C. X. Cardoso, M. F. S. Teixeira, *Sensor Actuat. B-Chem.* **2021**, *343*, 130141.
[12] a) A. G. Ayankojo, J. Reut, V. Syritski, *Biosensors-Basel* **2024**, *14*, 71; b) S. Dietl, H. Sobek, B. Mizaikoff, *Trac-Trend Anal Chem* **2021**, *143*, 116414; c) J. Marfà, R. R. Pupin, M. P. T. Sotomayor, M. I. Pividori, *Anal. Bioanal. Chem.* **2021**, *413*, 6141; d) S. A. Piletsky, N. W. Turner, P. Laitenberger, *Med Eng Phys* **2006**, *28*, 971; e) E. Mazzotta, T. Di Giulio, C. Malitesta, *Anal. Bioanal. Chem.* **2022**, *414*, 5165; f) G. Pilvenyte, V. Ratautaite, R. Boguzaite, S. Ramanavicius, C. F. Chen, R. Viter, A. Ramanavicius, *Biosensors-Basel* **2023**, *13*, 620; g) R. Singh, M. Singh, *Microchem. J.* **2025**, *215*, 114314; h) S. Akgönüllü, S. Kiliç, C. Esen, A. Denizli, *Polymers-Basel* **2023**, *15*, 629.
[13] E. Blasco, M. Piñol, C. Berges, C. Sánchez-Somolinos, L. Oriol, *Smart Polymers and their Applications*, Woodhead Publishing, Cambridge **2014**, pp. 510–548.
[14] M. F. S. Teixeira, M. M. Barsan, C. M. A. Brett, *RSC Adv.* **2016**, *6*, 101318.
[15] K. Bujak, H. Orlikowska, J. G. Malecki, E. Schab-Balcerzak, S. Bartkiewicz, J. Bogucki, A. Sobolewska, J. Konieczkowska, *Dyes Pigments* **2019**, *160*, 654.
[16] A. Gafiullina, B. P. Ladewig, J. J. Zhang, *ACS Appl. Polym. Mater* **2022**, *5*, 1.
[17] K. E. Edwards, M. Kim, T. H. Borchers, C. J. Barrett, *Mater. Adv.* **2022**, *3*, 6222.
[18] A. Ben Hassine, N. Raouafi, F. T. C. Moreira, *Chemosensors* **2021**, *9*, 238.
[19] A. Olean-Oliveira, T. Olean-Oliveira, A. C. R. Moreno, P. M. Seraphim, M. F. S. Teixeira, *ACS Sens.* **2019**, *4*, 118.
[20] A. Olean-Oliveira, P. M. Seraphim, M. F. S. Teixeira, *Electrochem. Commun.* **2022**, *136*, 107242.
[21] a) F. Lisdat, D. Schäfer, *Anal. Bioanal. Chem.* **2008**, *391*, 1555; b) E. P. Randviir, C. E. Banks, *Anal Methods-Uk* **2022**, *14*, 4602; c) A. Herrera-Chacón, X. Cetó, M. del Valle, *Anal. Bioanal. Chem.* **2021**, *413*, 6117.
[22] F. C. B. Fernandes, M. S. Góes, J. J. Davis, P. R. Bueno, *Biosens. Bioelectron.* **2013**, *50*, 437.
[23] a) P. R. Bueno, *Electrochim. Acta* **2023**, *466*, 142950; b) J. P. Piccoli, A. Santos, N. A. Santos, E. N. Lorenzón, E. M. Cilli, P. R. Bueno, *Biopolymers* **2016**, *106*, 357; c) A. Baradoke, A. Santos, P. R. Bueno, J. J. Davis, *Biosens. Bioelectron.* **2021**, *172*, 112705.
[24] M. A. MacDonald, H. A. Andreas, *Electrochim. Acta* **2014**, *129*, 290.
[25] P. R. Bueno, J. J. Davis, *Anal. Chem.* **2014**, *86*, 1997.
[26] a) P. C. M. Pizzol, M. L. Portugal, H. F. Trevizan, P. M. Seraphim, M. F. S. Teixeira, *Acs Appl Electron Ma* **2025**, *7*, 3486; b) T. Serra, S. Nieddu, S. Cavalera, J. Pérez-Juste, I. Pastoriza-Santos, F. Di Nardo, V. Testa, C. Baggiani, L. Anfossi, *Sensor Actuat B-Chem* **2025**, *428*, 137249; c) F. Bettazzi, A. R. Natale, E. Torres, I. Palchetti, *Sensors-Basel* **2018**, *18*, 2965.
[27] M. Cieplak, K. Szwabinska, M. Sosnowska, K. C. C. Bikram, P. Borowicz, K. Noworyta, F. D'Souza, W. Kutner, *Biosens. Bioelectron.* **2015**, *74*, 960.
[28] G. H. Zhang, Y. Yu, M. Guo, B. X. Lin, L. Zhang, *Sensor Actuat B-Chem* **2019**, *288*, 564.
[29] Z. Stojanovic, J. Erdossy, K. Keltai, F. W. Scheller, R. E. Gyurcsányi, *Anal. Chim. Acta* **2017**, *977*, 1.
[30] N. I. Wardani, P. Kanatharana, P. Thavarungkul, W. Limbut, *Talanta* **2023**, *265*, 124769.
[31] S. C. Patrick, R. Hein, P. D. Beer, J. J. Davis, *J. Am. Chem. Soc.* **2021**, *143*, 19199.
[32] C. Che, V. Gueskine, M. Sjödin, A. Pozhitkov, L. Yao, M. Berggren, Y. Ma, R. Crispin, M. Vagin **2025** Probing a conducting polymer by proton-coupled electron transfer of biosimilar redox molecules. New Journal of Chemistry, *49*, 4178–4190 https://doi.org/10.1039/d4nj04718d.